REGULAR PAPER

Bendability enhancement of 3D interconnections with out-of-plane corrugation for flexible hybrid electronics

To cite this article: Chang Liu *et al* 2024 *Jpn. J. Appl. Phys.* **63** 04SP74

Japanese Journal of Applied Physics 63, 04SP74 (2024)
https://doi.org/10.35848/1347-4065/ad375f

REGULAR PAPER

Bendability enhancement of 3D interconnections with out-of-plane corrugation for flexible hybrid electronics

Chang Liu[1*], Tadaaki Hoshi[1], Jiayi Shen[1], Atsushi Shinoda[1], Hisashi Kino[1,2], Tetsu Tanaka[1,2], and Takafumi Fukushima[1,2*]

[1]Graduate School of Engineering, Tohoku University, 6-6-1, Aoba, Aramaki, Aoba Ward, Sendai 980-8579, Japan
[2]Graduate School of Biomedical Engineering, Tohoku University, 6-6-1, Aoba, Aramaki, Aoba Ward, Sendai 980-8579, Japan

[*]E-mail: link@lbc.mech.tohoku.ac.jp

Received October 12, 2023; revised February 26, 2024; accepted March 25, 2024; published online April 22, 2024

This study focuses on enhancing the bendability of flexible interconnects with out-of-plane corrugation for flexible hybrid electronics. We propose two typical configurations of 3D corrugated interconnects: serpentine and trapezoidal. Three methods are introduced to fabricate these corrugated interconnects. The advantages and drawbacks of each fabrication strategy are discussed, and the impact of the 3D corrugation geometry and material on bendability is elucidated. In addition, the material properties of two types of negative photosensitive materials, SU-8 and F-PD (flexible-photoimageable dielectric), are compared. Results show that the resistance increase of 3D corrugated interconnects after a 5 mm radius bending test is drastically lower (by approximately 1900%–2000%) than that of conventional 2D planar interconnects.

1. Introduction

Flexible hybrid electronics (FHE) are a new category of electronics; they consist of devices that combine the flexibility of wire-printed plastic film substrates with the performance of semiconductor Si or III–VI devices.[1,2) Conventional FHE is fabricated by mounting ultrathin dies on the surfaces of polymeric sheets, where each component is interconnected by printable wires.[3] Ultrathin dies are 5–10 times thinner than ordinary dies and thus have higher flexibility. However, the electrical performance of ultrathin dies can degrade and fluctuate. In addition, the thickness[4,5] and density[6] of printable wires are limited by their fabrication process.

An essential topic in FHE is their interconnections, which determine the duration and reliability of FHE functionality. Flexible interconnects have three contemporary designs: wavy and wrinkled, origami/kirigami-inspired, and island–bridge designs. The wavy, wrinkled design was initially developed to create stretchable single-crystal silicon electronics on rubber substrates.[7] This design involves introducing strain into a soft substrate (e.g. silicone) through thermal expansion[8] or mechanical prestretching[9] and using this prestrain to form wavy patterns in a hard film (e.g. metals or semiconductors). Researchers have explored the use of heterogeneous bilayer substrates to develop approaches that balance stretchability and robustness.[10–12] However, these methods have drawbacks. They require precise prestraining, which adds technical challenges and costs. Prestrained substrates can also complicate die packaging and alignment with interconnects. These strategies are unsuitable for scaling down the density of flexible wires.

The second approach is derived from origami and kirigami, or the ancient art of paper folding and cutting, respectively; such methods were adopted recently by Cheng et al.[13] and Song et al.[14] to enhance the deformability and areal energy density of stretchable batteries. This approach incorporates concepts from manual origami, where parallelogram faces are interconnected by “mountain” and “valley” creases. When subjected to external loads, these parallelogram faces generally remain undeformed while the creases fold and unfold, leading to strain concentration in the crease regions. The critical challenge in this method is minimizing strain levels in crease regions to prevent material fracture or plastic yielding. Due to the complex 3D geometry of origami structures, analytical modeling primarily focuses on a subset of mechanical properties, such as bending rigidity and Poisson ratios.[15,16] Detailed deformation and strain distribution analyzes rely mainly on finite element analysis (FEA).[17] However, a notable limitation of this strategy is its scalability in advanced microelectronic applications. As electronics are miniaturized, theoretical analysis becomes less effective in understanding the intricate mechanics of such devices, making deformation control more challenging during fabrication. Additionally, structures with this design may not be universally applicable, as they may be incompatible with existing functional dies, particularly concerning alignment and bonding.

The island–bridge design, initially proposed by Lacour et al., aligns well with conventional electronics design principles.[18] This design comprises rigid islands, rigid dies, and flexible interconnects (bridges) in which wavy wires connect active devices. The rigid islands, which have high effective stiffness, remain nearly undeformed (<1% strain) to maintain the mechanical integrity of functional inorganic semiconductor materials. The interconnects, which have lower effective stiffness, deform to provide flexibility. The bridge structure design is a crucial aspect, as it determines essential mechanical properties, such as Young’s modulus and stretchability.

According to bridge geometry, island–bridge designs can be further categorized into three groups: straight, serpentine, and fractal-inspired interconnects. In island–bridge designs, straight interconnects can be firmly bonded (via chemical covalent bonding) or weakly bonded (via van der Waals interactions) to prestretched elastomeric substrates, resulting in wavy coplanar interconnects or arc-shaped noncoplanar interconnects upon prestrain release.[19] Unlike wavy, wrinkled wires, this design focuses on arc-shaped noncoplanar interconnects. Lateral buckling may occur, including bending and twisting deformation, causing shear stress in wires.

Designs with serpentine interconnects are more flexible than those with straight ones, even without applying any prestrain to elastomer substrates. Offering high flexibility without needing prestrain in such substrates, serpentine interconnects can be fully bonded, partially bonded, or nonbonded to substrates, depending on application requirements. Vertical space is required for deformation, limiting the possibility of overlaying multiple layers in certain applications.

The fractal-inspired interconnect design was introduced to create ultrastretchable lithium-ion batteries;[20] this design is used in various stretchable bioelectronic devices.[21,22] It optimizes the limited space in a device by increasing the fractal order, thus enhancing the overall coverage of functional components and overall stretchability. FEA is the primary method used to study the deformation tendencies and stress distributions of these devices. However, further research is needed to understand their pattern designs and deformation mechanisms.

We propose a structurally new FHE to address the abovementioned wire density, functional degradation, and fabrication issues.[23–25] The device uses inorganic single-crystal semiconductors, especially Si, and does not use organic, amorphous, or polycrystalline semiconductors. This concept is influenced by conventional 2D serpentine wire designs[26] and leverages a previously proposed 3D interconnect technology.[27] 2D serpentine wires have been developed, but their density is limited by their structural design and printing process.[26] Our previous work featured a polymer slope that allowed interconnects to ascend 100 μm thick Si dies, but the structure had no flexibility.[27] By contrast, the present study deals with flexible 3D corrugated interconnects fabricated through fan-out wafer-level packaging (FOWLP). This study primarily aims to enhance device bendability by designing and fabricating interconnects with vertically corrugated configurations. Moreover, the effectiveness of photosensitive resins with low Young's moduli and alkaline-soluble functional groups is described in terms of the formation of 3D corrugation patterns and bending properties.

2. Experiment

2.1. Materials

In this work, polydimethylsiloxane (PDMS) was used (Dow Corning Silastic™ MDX4-4210). The base resin and curing agent were mixed in a weight ratio of 1:10 using a planetary centrifugal mixer (Thinky ARE-310). Thermal release tapes Rivalpha RA 95 L(N) and 3195 V (Nitto Denko) were utilized as the first and second temporary adhesion layers, respectively. RA 95 L(N) and 3195 V lose adhesion in 1 min when heated at 95 °C and 170 °C, respectively. A Parylene C stress buffer layer was deposited via chemical vapor deposition (Specialty Coating Systems PDS2010). We used two types of photosensitive dielectrics to form 3D corrugated patterns. Negative photosensitive resins (SU-8 3025 and SU-8 3005) were obtained from Nippon Kayaku. Taiyo Ink Manufacturing provided a flexible photoimageable dielectric (F-PD), a transparent photosensitive material. Two types of adhesion promoters were employed. Hexamethyldisilazane (HMDS) was from Tokyo Ohka Kogyo, and KBM-403 was from Shin-Etsu Chemical.

2.2. Measurement

Photomicrographs were taken using a digital microscope (Keyence VHX-8000). Scanning electron microscopy images were obtained using a scanning transmission electron microscope (Hitachi SU-70). Film thicknesses and surface profiles were characterized using a contact-type surface profiler (Kosaka Laboratory ET200). Bending tests were conducted using a U-shaped folding test machine (Yuasa System Tension-Free™ U-shaped folding tester). The electrical properties of the interconnect were characterized using a manual probe station system (Micronics 708fT) and a semiconductor device parameter analyzer (Keysight Technologies B1500A).

2.3. Simulation

The interconnect dimensions were determined based on static structure simulation[28–30] results computed using Ansys Workbench. Two typical configurations of corrugated interconnects were designed, as shown in Fig. 1.

2.4. Fabrication

Figure 2 shows the fabrication process. The first handler was formed by laminating the thermal release tape RA 95 L(N) on a 1 mm thick double-side-polished Si wafer. A mixed PDMS base resin with a curing agent, whose weight was determined to prevent overflowing, was poured on the handler and trapped using a 0.5 mm thick Teflon ring. The structure was vacuum defoamed at an absolute pressure of <6.3 kPa for approximately 10 min in a bell jar to diminish voids in the PDMS base generated when the sandwich structure compressed the uncured fluid PDMS. During the initial defoaming process, we repeatedly vented the bell jar to quickly remove air bubbles dissolved in PDMS due to pressure changes. When the high-viscosity liquid PDMS had no visible bubbles on its surface, the second handler was created by laminating the other thermal release tape (3195 V) on a 1 mm thick double-side-polished Si wafer with the help of a weight. The PDMS weight was approximately 0.7253 g. The sandwich structure was defoamed for an additional 15 min and cured at 40 °C and in an atmospheric environment for 24 h. After PDMS was cured sufficiently, the sandwich-structured sample was thermally debonded at 95 °C on a hot plate. We then deposited the 1 μm thick Parylene C SBL[31] to alleviate the thermal expansion of PDMS. The Parylene C surface was modified using a VUV/O_3 irradiation unit (Ushio

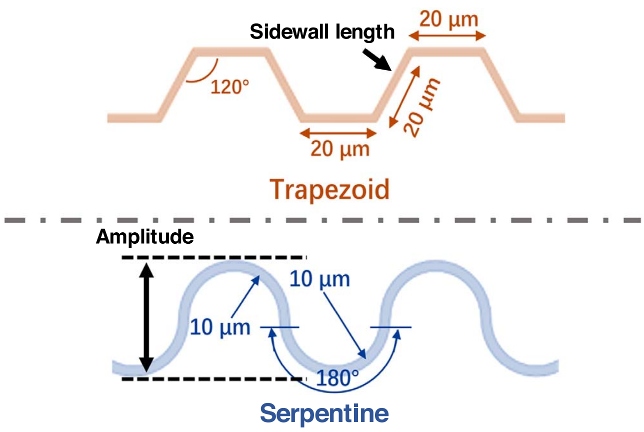

Fig. 1. Design of out-of-plane configurations for 3D corrugated interconnects.

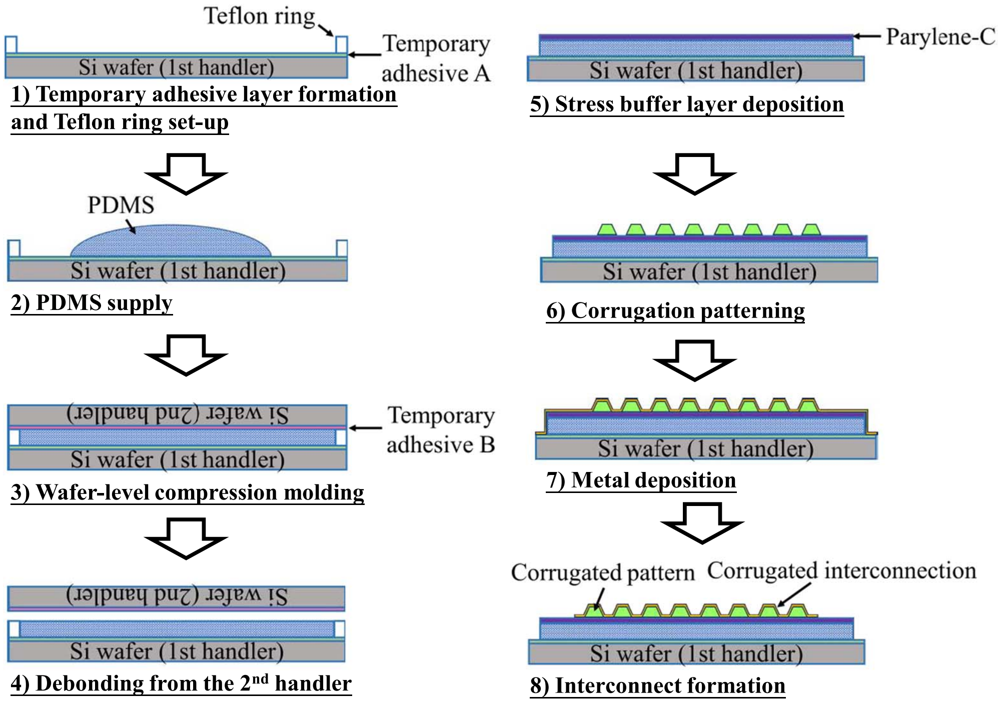

Fig. 2. Fabrication process of 3D corrugated interconnects.

NEX-V-172) at a wavelength of 172 nm to remove possible organic contaminants and increase its hydrophilicity. Adhesion promoters for SU-8 and F-PD were applied to render high hydrophilicity on the surface and to enhance the adhesion strength between Parylene and photosensitive materials. We employed HMDS for F-PD. For SU-8, we used a silane coupling agent with epoxy groups adhesion promoter KBM-403 because, according to the stud-pull test, the bonding strength promoted by KBM-403 between SU-8 and Parylene is 0.46Mpa, approximately 20% higher than the case of HMDS (0.38 MPa). Then, a negative photosensitive material (SU-8 3025 or F-PD) was spin coated and patterned using a g-line UV photolithography system (SUSS MicroTec MA6) through the following method. We irradiated the fully cured SU-8 3025 or F-PD corrugation using the VUV/O_3 irradiation unit to enhance the adhesion between the metallization layer and 3D corrugated patterns. Next, a Ti/Au/Ti film with layer thicknesses of 50, 500, and 50 μm, respectively, was deposited; the Ti layer served as an organic/metal adhesion layer.[32–34] The interconnects were formed through wet etching using buffer fluoric acid (hydrofluoric acid/ammonium fluoride/water, 10/95/95 ml) for Ti and using 1/4.2 wt% iodine complex/potassium iodine for Au.

3. Results and discussion

3.1. Bending stress simulation

The simulated bending test is shown in Fig. 3. Two fixtures hold both ends of the PDMS-based structure in the length direction. The structure bends spontaneously as the fixtures approach each other. The PDMS structure has a much lower Young's modulus during displacement than the other materials used in the structure, so it compresses before the other layers. As the fixtures approach each other, PDMS compression continuously increases, thus stretching the upper metallization layer. Under such simulated boundary conditions, the structure bends in only one steady state, and the metallization layer always stretches instead of compressing.

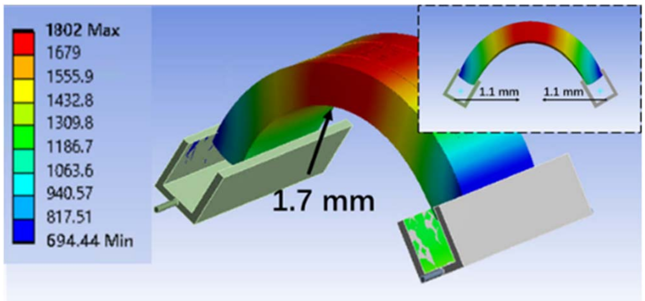

Fig. 3. Mechanical simulation setup of bending test in Ansys.

The left graph in Fig. 4 presents the relationship between the maximum stress and wire thickness. With an increase in wire thickness, the maximum von Mises stress grows almost linearly for both serpentine and trapezoidal configurations. The maximum stress of the serpentine configuration tends to be larger than that of the trapezoidal configuration, but the difference is not significant. The maximum stress in corrugated wires is always smaller than the tensile strength, which is defined as Eq. (1)[35]

$$\sigma_{\mathrm{YS}} = 129.2 + 119.3t^{-\frac{1}{2}}, \tag{1}$$

where σ_{YS} is the yield strength of the metal film and t is the thickness of the metal film. σ_{YS} only relates to the thickness because at high yields, thickness-independent interface toughness no longer holds, and the wire deforms highly nonlinearly. Therefore, small-scale yield cannot be achieved with a film thickness of <100 μm. On the contrary, the simulation results of 2D planar wires are more significant than the tensile strength of the metal film regardless of thickness, proving that the corrugated wires indeed improve the bendability of the structure. In the right graph, an increase

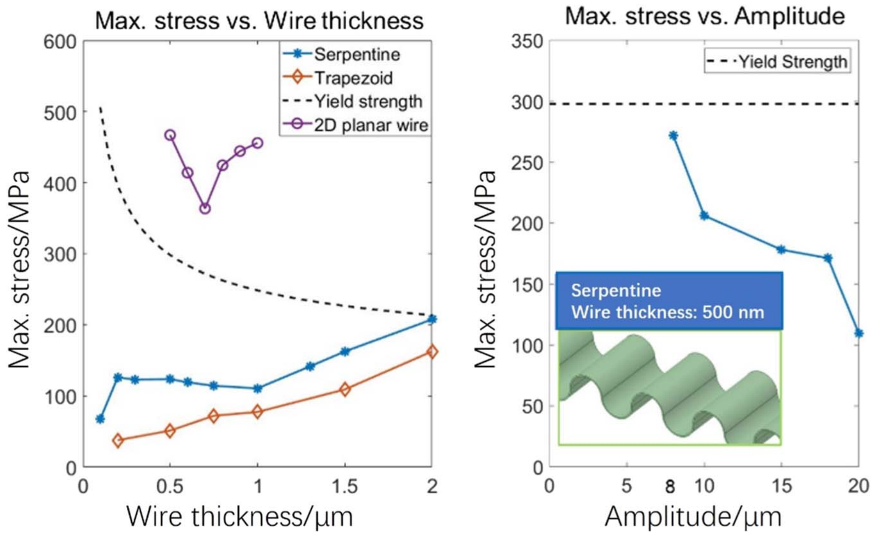

Fig. 4. Simulation results of maximum stress versus wire thickness and amplitude.

in the corrugation amplitude reduces the maximum stress. This may be because the total wire length increases with the corrugation amplitude. When the wires are stretched at the same displacement, longer wires exhibit smaller strain. These simulation results guide the dimensional design in the fabrication process.

3.2. Fabrication strategies for 3D corrugation

Three methods were used to fabricate the proposed 3D corrugated structures using SU-8.

3.2.1. Proximity gap control. The standard photolithography process, which involves mask aligners, usually uses a hard/soft contact mode, indicating a proximity gap of approximately 0 μm between the photomask and the photoresist during UV irradiation. This enhances accuracy in transferring patterns from the former to the latter. However, the vertical sidewalls of the dielectric patterns contradict the structure design because the sharp corners contribute to high-stress concentration when wire patterns are formed on the sheer corrugation.

As the proximity gap grows, as demonstrated in Fig. 5, the highly parallel UV light generated by the aligner is diffracted after going through the Cr patterns. Consequently, the photoresist has sloped sidewalls. Notably, the diffracted UV light has a lower intensity than direct light. Thus, the photoresist in the sloped regions will be insufficiently exposed if the exposure time is calculated based on the standard dose, resulting in structural defection and delamination. Therefore, additional exposure time is required to ensure sufficiently strong cross-linking to bond the photoresist to the bottom layer (Parylene C).

The controlled high-exposure-dose strategy enlarges the proximity gap between the photomask and the photoresist to enable the diffraction of UV light, thus generating sloped sidewalls. The trapezoidal configuration is formed using this method. The SU-8 patterns fabricated via this method are shown in Fig. 6. The exposure dose was 450/750 mJ cm^{-2}. The sidewall tilt of the SU-8 patterns ranges from 23° to 70°. When adjacent patterns are too close, the SU-8 material cross-links due to the diffracted UV light. This narrows the space region, thus preventing the corrugation from uniformly forming valleys and peaks. This problem can be solved by increasing the space between adjacent patterns, but this will also increase the pitch, making it difficult to scale down the corrugation. Besides, the pattern parts exposed to the diffracted UV light are not fully cross-linked, as seen in Fig. 6(c). The pattern transparency varies, indicating nonuniform cross-linking. Furthermore, SU-8 is sensitive to proximity gaps. Figure 6(e) presents the SU-8 sample fabricated using a 30 μm proximity gap. All patterns merge; that is, the spacing disappears. However, because the exposure dose is not high, the pattern heterogeneity increases because some parts are insufficiently exposed. This is a tradeoff of this technology.

3.2.2. Use of grayscale photomask. The intensity variation of the Cr patterns on the photomask can be adjusted to regulate the amount of UV light that passes through. If the photoresist region uncovered by the photomask is exposed to

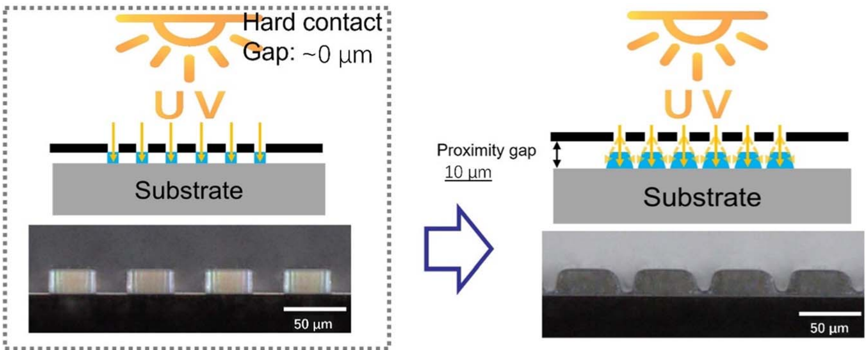

Fig. 5. Mechanism of proximity gap control.

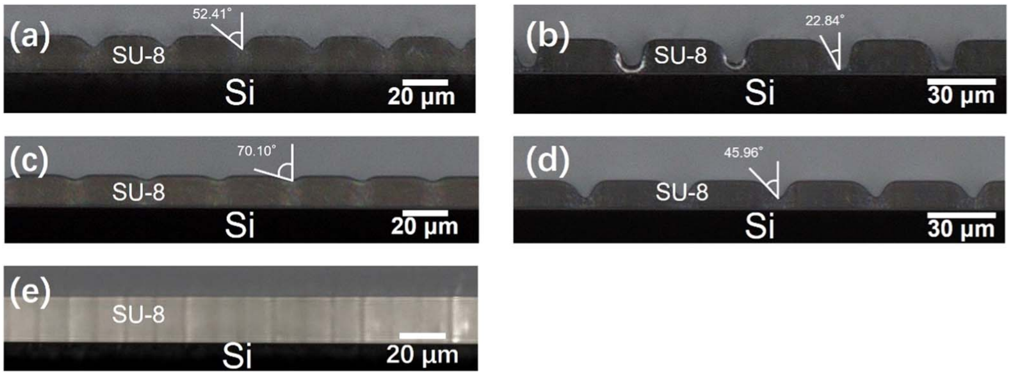

Fig. 6. SU-8 corrugation patterns fabricated under various processing conditions of proximity gap control at high exposure doses; the pitch of corrugated patterns on the photomask: 40 μm (a), (c), (e) and 60 μm (b), (d), proximity gaps: 10 μm (a)–(d) and 30 μm (e), and exposure doses: 450 mJ cm^{-2} (a), (b), (e) and 750 mJ cm^{-2} (c), (d).

different UV light doses formed by a grayscale mask, and then, the desired corrugation profile can be obtained through standard photolithography. Figure 7 schematically illustrates the mechanism of the grayscale photomask and how it guides the UV light intensity distribution. In this work, instead of patterns composed of binary transparent and opaque parts of the photomask whose shapes are identical to that of the desired pattern, we use designs on a grayscale photomask consisting of uniform units (dots) sized 1 or 2 μm that can tune the amount of UV light by varying its intensity.

Using a grayscale photomask is an optional method for forming the desired configuration. By tuning the distribution of the dots constituting the corrugation patterns, we fabricate two types of Cr grayscale photomasks. The first one comprises 1 μm diameter dots, and the other comprises 1- and 2 μm diameter dots. Figure 8 shows optical photos of the two grayscale photomasks; a plain photomask has only opaque and transparent parts. However, the transmission of UV light through the grayscale photomask and its intensity distribution are not explored adequately. The UV light that reaches an SU-8 layer depends not only on the designed pattern on the photomask but also on factors such as the thickness of the photoresist film and the mechanical properties of the exposed photosensitive dielectric. Additionally, a thick film needs a higher exposure dose to be fully exposed; this requires extra diffracted UV light, resulting in pattern overexposure. The use of a grayscale photomask in design is complex and requires photolithographic simulation and experimentation, but optimization is not performed in this work.

The fabrication results are shown in Fig. 9. If photolithography is conducted without a proximity gap, then the dot patterns will be transferred from the photomask to SU-8, thus roughening the corrugation pattern surfaces. If SU-8 has reflowable properties when heating, then the roughened patterns will be smoothed. However, the shapes of the photo-cross-linkable SU-8 patterns are not rounded after they are heated at 120 °C–180 °C at the postbaking temperature of SU-8. Unless the photosensitive dielectric used to fabricate the 3D corrugation has a high softening point of above 120 °C, the upper temperature restricts the entire fabrication. PDMS substrates become unstable and expand significantly due to their large coefficient of thermal expansion. Therefore, the fabrication process should be conducted

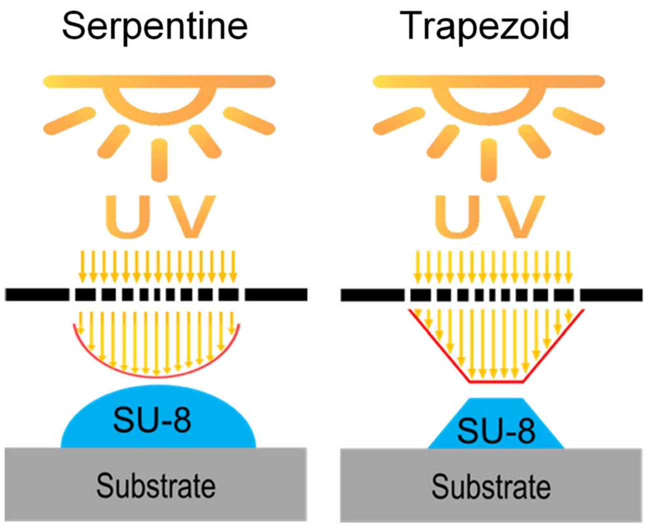

Fig. 7. Schematic diagram of mechanism of photolithography using grayscale photomask.

at low temperatures (<120 °C). Another possible option is to defocus the lens of the aligner (i.e. enlarge the proximity gap), as previously mentioned. The defocused UV light will be diffracted, thus easing the intensity variation and smoothing waves or dots.

As shown in Fig. 9, both serpentine and trapezoidal corrugation patterns can form under different photolithography conditions. However, the patterned SU-8 shows considerable heterogeneity, as seen in Fig. 9(c). This is attributed to the unsmooth transition of the dot distribution on the grayscale photomask from the opaque region to the transparent region. Here, the spatial resolution of Cr photomask fabrication is limited to roughly 1 μm. However, the need to fabricate symmetric corrugation with a pitch of less than 40 μm gives us a space of less than 10 μm to adjust the dot density distribution, indicating that no more than 10 variations can be obtained. Furthermore, in the case of the trapezoidal configuration, positively sloped planar sidewalls are preferable. However, due to the nonlinearity of SU-8 exposure concerning the dot distribution, designing a grayscale photomask capable of fabricating patterns with perfectly linear sidewalls is challenging. Fabricating patterns with desired serpentine and trapezoidal configurations using a perfect grayscale photomask requires further optimization, which is not yet feasible.

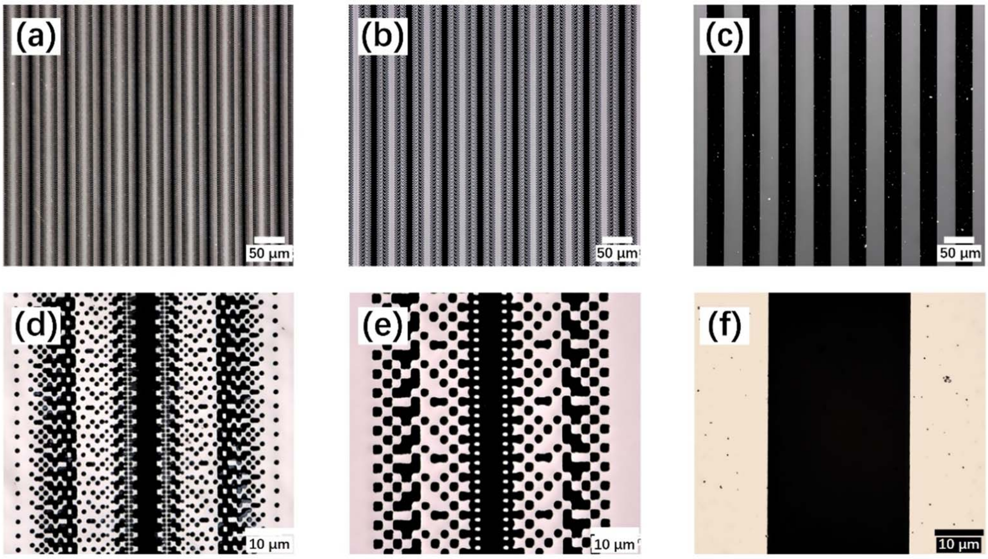

Fig. 8. 3D corrugation patterns formed using grayscale photomasks with various pitch sizes and proximity gaps: (a), (d) serpentine configuration; (b), (c), (d), (f) trapezoidal configuration.

Fig. 9. Cr grayscale photomasks consisting of dots with different diameters and a plain photomask for comparison. Overview of patterns on grayscale photomasks with (a) 1 μm diameter dots and (b) 1- and 2 μm diameter dots; (c) plain photomask with only opaque and transparent parts; (d), (e), (f) magnified views of (a), (b), and (c), respectively.

3.2.3. Overlay coating (double-layered coating). The capillary forces acting during coating and drying produce a certain accumulation of catalysts at spacing corners.[36] During the spin coating of another thin film of SU-8, the existing SU-8 patterns, which have vertical sidewalls and sharp edges and are fabricated through standard photolithography, will be rounded by the accumulated overlaid SU-8 by the capillary forces acting in the narrow spaces between adjacent patterns. The SU-8 material used for the prior (existing) patterns is SU-8 3025 (viscosity: 4.4 Pa·s; coating thickness: 20 μm), and the overlaid material is SU-8 3005, which has lower viscosity (0.065 Pa·s), enabling the formation of SU-8 in the spaces.

Unlike the two other methods for 3D corrugation fabrication, overlay coating is more controllable and less complicated; the SU-8 3005 diluted at different concentrations in the spaces is attributed to the capillary effect. Figure 10 shows the rounded spacing regions under different fabrication conditions. As the concentration of the diluted SU-8 3005 increases, the valley part between adjacent patterns accumulates thicker SU-8. The optimal thickness pattern of the spacing region is supposed to be rounded. The thickness of the center part should be half the height of existing vertical-sidewall patterns to form the target shape, as demonstrated in Fig. 1, in which the target shape is accomplished by using 80:20 diluted SU-8 3005, spin coating at 1000 rpm can be achieved, as shown in Fig. 10. Meanwhile, the photoresist accumulation in the valleys is noticeably more significant than that in the peak regions. In the valley parts, the additional SU-8 is restrained by the existing patterns. In the peak regions, due to the contact area limitation and lack of constraints, SU-8 keeps the volume very small during additional spin coating. Therefore, the peaks are not rounded substantially, unlike the valleys. This issue may be solved by enhancing the surface adhesion between the overlaid and prior SU-8 using adhesion promoters or using a spray coater instead of a spin coater to eliminate the influence of centrifugal forces on the coated SU-8. Nevertheless, the patterns are noticeably heterogeneous due to the density difference between SU-8 3025 and 3,005. Although heating the sample beyond the glass transition temperature (200 °C for SU-8) may solve this issue, this is not feasible for PDMS substrates. Therefore, this inevitable problem influences the mechanical properties of serpentine patterns fabricated via this method.

3.3. Material strategies for forming 3D corrugation

In our previous work,[24] we utilized SU-8 as a photosensitive dielectric for corrugation. As shown in Table I, the mechanical properties of the SU-8 patterns are also uncertain due to the density distribution. SU-8 is a brittle material. After curing, cracks tend to appear in regions where the cross-link density varies; thus, fabricating trapezoidal configuration patterns using proximity gap control with SU-8 is not an optimal option. We therefore explore F-PD as an alternative negative photosensitive dielectric. Compared with SU-8, F-PD has a lower Young's modulus, which helps increase the

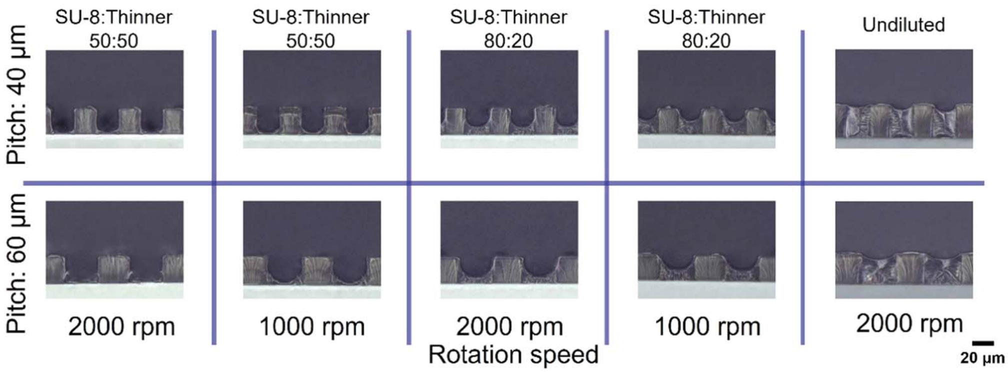

Fig. 10. Overlay coating results. Two main rotation speeds are used for overlay coating. An SU-8 thinner is used to dilute SU-8 3005 (which has a different solids ratio) because its viscosity is relatively high for such a method. The results for undiluted SU-8 3005 are shown in the rightmost column. It nearly fills the spaces between adjacent patterns.

Table I. Material characteristics of SU-8 and F-PD.

Properties	SU-8	F-PD
Young's modulus	2.0 GPa	1.0–1.2 GPa
Curing temp.	150–200 °C	130 °C
Developer	Organic	Alkaline (2.38% TMAH:H2O 1:15 vol%)

flexibility of the whole structure. The curing temperature of F-PD is also much lower than that of SU-8 so that the fabrication process can be completed at a low temperature (<120 °C). To fabricate sloped sidewalls as a trapezoidal configuration and fully irradiate the photosensitive F-PD, we adopt our proximity gap control and high-exposure-dose strategies (Sect. 3.2.1). Figure 11 shows the trapezoidal patterns created using F-PD at a 900 mJ cm^{-2} exposure dose (three times the standard dose), a 30 μm proximity gap, and 3 min puddle development with 2.38% tetramethylammonium hydroxide (TMAH) diluted using a 15-fold volume of water. These trapezoids have clearly sloped sidewalls that tilt at an angle of approximately 120°, which is consistent with the design configuration. Compared with the SU-8 patterns, the F-PD patterns do not exhibit prominent density variations, ensuring the uniformity of mechanical properties.

The detailed composition of F-PD has not been released. Nevertheless, we can give a hypothesis explaining why it can form the desired corrugation using the proximity gap and exposure dose control methods. A specific organic

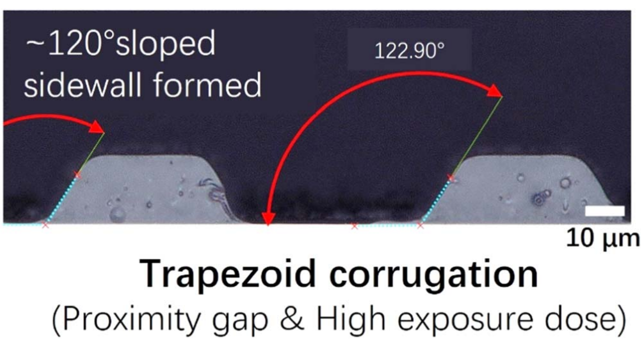

Fig. 11. Corrugation fabrication results using F-PD. The trapezoidal corrugation is formed via proximity gap control at a high-exposure-dose. The sidewalls of the corrugated patterns are tilted by approximately 120°, consistent with the design specifications. The cross-sectional view does not show prominent heterogeneity between patterns.

developer is used for the development process of SU-8. It also has many epoxy groups. After cross-linking, the solubility rate of irradiated SU-8 against its organic developer reduces considerably, as illustrated in the left-hand part of Fig. 12. By contrast, F-PD was originally formulated using a developer of 1 wt% Na_2CO_3, an extremely weak alkaline solution. However, sodium ions are unsuitable for semiconductor fabrication. Therefore, we replaced it with a 2.38% TMAH solution diluted using a 15-fold volume of water to establish an analogous alkaline environment. The F-PD chemical structure is assumed to include carboxyl and/or hydroxyl functional group residues, which strongly react with the TMAH developer through ionic interactions, as shown in the right-hand part of Fig. 12, although the material is cross-linked via radical polymerization. Figure 13 schematically illustrates the difference between the SU-8 and the F-PD processes. The irradiated part can still be dissolved in the developer, showing no significant solubility compared with nonirradiated parts. Hence, time is crucial during development. If the time is insufficient, then the development will be inadequate, and patterns will contact each other. On the contrary, if the development time exceeds certain limitations, then the irradiated part will also dissolve in the developer; patterns will start delaminating from the substrate because of the decline in adhesion resulting from the alkaline solvent penetrating the interface between the irradiated patterns and substrates. The formation of the trapezoidal patterns (Fig. 2) also depends on the pitch and the film thickness of the photosensitive material. The trapezoidal configuration is only successfully fabricated at a patterning pitch of 60 μm when the film thickness after the spin coating is 20 μm and shrinks to approximately 18 μm after 20 min soft baking at 80 °C. The development time needed for the aforementioned fabrication conditions is 2–3 min at 23 °C. The development time largely affects the resulting shape of F-PD.

3.4. Bendability

The bendability of the 3D corrugated interconnects based on the PDMS substrate is evaluated using an endurance testing system (tension-free U-shaped folding tester). Figure 14(a) shows the resistance change of the 3D corrugated interconnects with serpentine and trapezoidal configurations. Au and Ti are selected instead of Cu for their high biocompatibility, as the target device needs long-term wearability. 3D corrugated interconnects with a line/space of 100/100 μm are

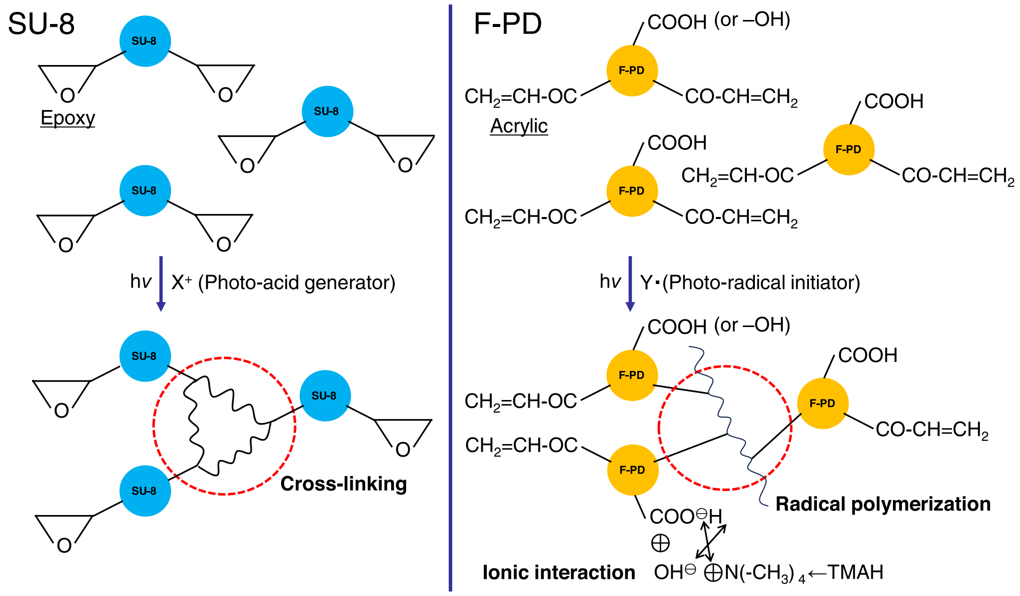

Fig. 12. Schematic of chemical reactions in the development process of SU-8 and F-PD. Once irradiated, the epoxy groups in SU-8 cross-link, and the solubility rate of irradiated SU-8 against the organic solvent reduces notably. On the contrary, the solubility of irradiated F-PD remains nonnegligible due to the high ionic interaction between irradiated F-PD's carboxylic acid and the TMAH developer.

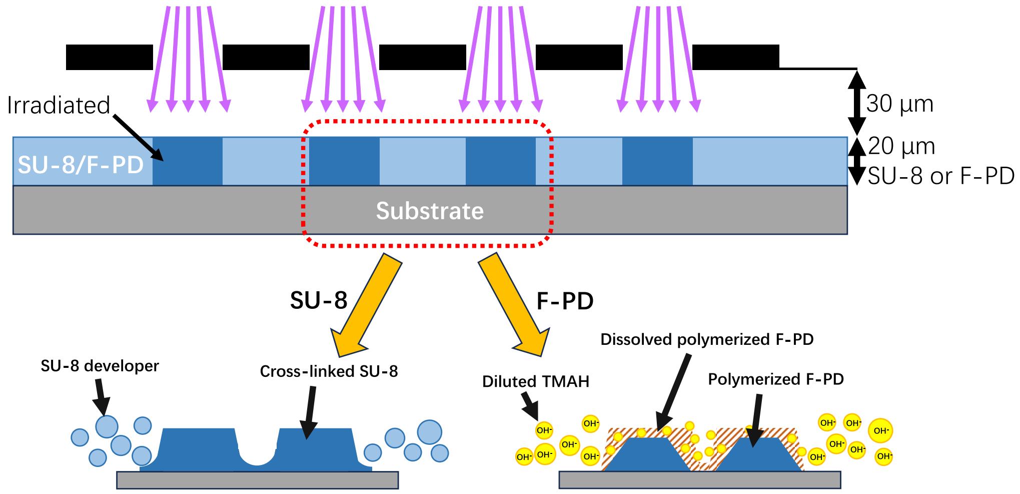

Fig. 13. Schematic illustration of the difference between SU-8 and F-PD process. SU-8's organic developer can only dissolve the nonirradiated SU-8. However, the solubility of irradiated F-PD does not differ from the nonirradiated part notably. The area, which is irradiated and exposed to diluted TMAH solution, will be dissolved so that a trapezoid configuration with larger tilted sidewalls will form.

chosen for comparison with 2D planar interconnects. The test samples are set on the bending tester, and U shapes are created by bending the samples (curvature radius: 5 mm) for 100 cycles. The resistances of the 2D and 3D interconnects are evaluated before and after the bending test. The result for the 3D wires with SU-8 corrugation shows that the trapezoidal configuration exhibits a lower resistance change than the serpentine configuration, which is consistent with the simulation results. A larger amplitude leads to this reduction in its resistance change; for example, 60 μm pitch corrugated wires mitigate the resistance increase by approximately 55% relative to 40 μm pitch ones. However, the trapezoidal configuration does not exhibit such a phenomenon. As for corrugated interconnects formed on pliable F-PD patterns with the trapezoidal corrugation, the resistance change dramatically reaches approximately 10%, mainly due to its low Young's modulus. Therefore, the stress-neutral plane is close to the metallization layer. Finally, despite the higher resistance increase of the SU-8 corrugated wires, the resistance change in all cases is significantly smaller than that of 2D planar wires, which exceeds 2000%. According to Fig. 14(b), after 100 cycles of the bending test, the corrugated interconnects with SU-8 exhibit no conspicuous morphological alterations, unlike the conventional 2D planar ones. On the contrary, the 2D planar wires shrink in some regions, resulting in a severe reduction in conductivity. Because of its structural design (avoids stress concentration), material elongation, and strain to yield stress, a 3D interconnect with F-PD corrugation shows excellent bendability, even when the wire is not covered with any protection layers to control the stress-neutral plane.

4. Conclusions

To address a critical issue regarding structurally new FHE created using FOWLP with small embedded dies, we developed highly bendable interconnects with 3D

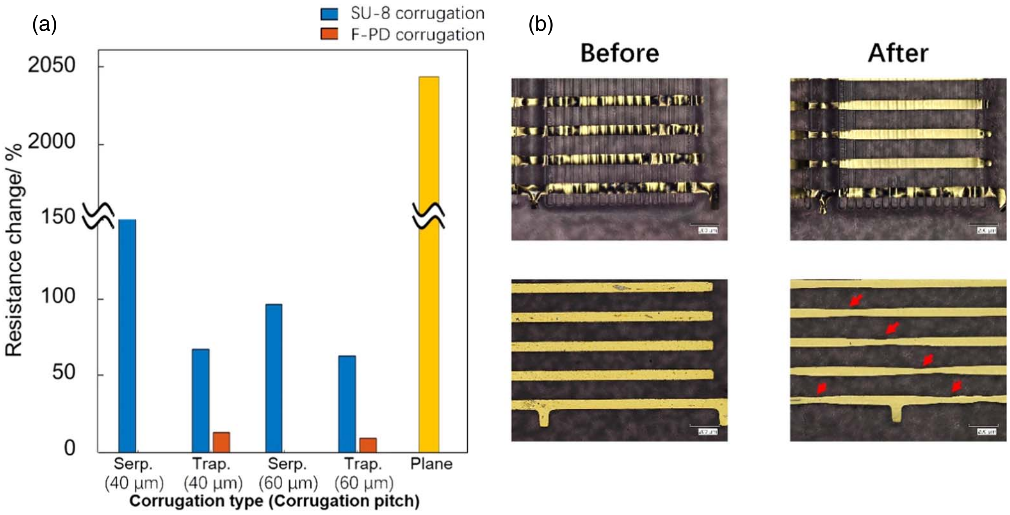

Fig. 14. Difference in resistance increase between 3D corrugated wires and conventional 2D planar wires after 100 cycles of bending (bending radius: 5 mm; bending speed: 30 rpm): (a) 3D corrugated wires formed on SU-8 and F-PD corrugation with 40/60 μm pitch and 2D planar wires with wire line/space of 100/100 μm. (b) 3D corrugated (top) and 2D planar (bottom) interconnects after the bending test; red arrows indicate the delaminated and shrunk parts.

corrugation. Several design parameters were determined by simulating the desired structure via FEA. Based on the rigid SU-8 results, the desired trapezoidal corrugation was able to be formed with proximity gap control and high exposure dose without much conditioning using F-PD. Furthermore, we found that chemical properties inherent to F-PD played a pivotal role in achieving our preferred outcomes for flexible trapezoidal patterns.

I–V characterization was conducted after the successful fabrication of the 3D corrugated interconnects. The results showed that the 3D corrugated interconnects had a significantly lower resistance increase induced by the bending test in comparison with conventional 2D planar interconnects (over 2000%). The resistance change of the SU-8 corrugated interconnect ranged from 70% to 150%. Due to F-PD's lower Young's modulus, the F-PD corrugated interconnect's resistance change was approximately 20%, which was only a third or lower of that of SU-8. Additionally, the larger corrugation pitch leads to relatively lower stress; the trapezoidal corrugated interconnects have smaller induced stress than the serpentine corrugated ones, consistent with the simulation findings. This work provides a platform for FOWLP-based FHE. The flexibility and durability of devices based on this technology will significantly improve. Our future work will be on finer-pitch corrugation formation, the formation of 3D interconnects with F-PD serpentine corrugations, and die/chip 3D interconnect bonding technologies.

Acknowledgments

This work was performed in the Micro/Nano-machining Research and Education Center (MNC) and Jun-ichi Nishizawa Research Center at Tohoku University. This work was supported by JSPS KAKENHI Grant Nos. 19KK0101, 21H04545, and 22K18291. This work was supported by JST SPRING, Grant No. JPMJSP2114. This work was supported by the Graduate Program for Integration of Mechanical Systems of Tohoku University. This work was also supported through the activities of VDEC, The University of Tokyo, in collaboration with Cadence Design Systems.

ORCID iDs

Chang Liu https://orcid.org/0000-0002-8574-2681

1) Y. Khan, A. Thielens, S. Muin, J. Ting, C. Baumbauer, and A. C. Arias, Adv. Mater. **32**, 1905279 (2020).
2) R. Herbert, J. H. Kim, Y. S. Kim, H. M. Lee, and W.-H. Yeo, Materials **11**, 187 (2018).
3) J. S. Chang, A. F. Facchetti, and R. Reuss, IEEE J. Emerg. Sel. Top. Curcuits Syst. **7**, 7 (2017).
4) S.-Z. Guo, K. Qiu, F. Meng, S. H. Park, and M. C. McAlpine, Adv. Mater. **29**, 1701218 (2017).
5) S. Zips, O. J. Wenzel, P. Rinklin, L. Grob, K. Terkan, N. Y. Adly, L. Weiß, and B. Wolfrum, Adv. Mater. Technol. **4**, 1800455 (2019).
6) P. Sun, J. Zhang, X. Zhu, H. Li, Y. Li, J. Yang, Z. Peng, G. Zhang, F. Wang, and H. Lan, Adv. Mater. Technol. **7**, 2200302 (2022).
7) D.-Y. Khang, H. Jiang, Y. Huang, and J. A. Rogers, Science **311**, 208 (2006).
8) N. Bowden, S. Brittain, A. G. Evans, J. W. Hutchinson, and G. M. Whitesides, Nature **393**, 146 (1998).
9) J. Jones, S. Lacour, S. Wagner, and Z. Suo, J. Vac. Sci. Technol. A **22**, 1723 (2004).
10) J. A. Rogers et al. (ed.) *Stretchable Bioelectronics for Medical Devices and Systems* (Springer, Cham, 2016) p. 53.
11) H. Cheng, Y. Zhang, K.-C. Hwang, J. A. Rogers, and Y. Huang, Int. J. Solids Struct. **51**, 3113 (2014).
12) H. Jiang, D.-Y. Khang, H. Fei, H. Kim, Y. Huang, J. Xiao, and J. A. Rogers, J. Mech. Phys. Solids **56**, 2585 (2008).
13) Q. Cheng, Z. Song, T. Ma, B. B. Smith, R. Tang, H. Yu, H. Jiang, and C. K. Chan, Nano Lett. **13**, 4969 (2013).
14) Z. Song, T. Ma, R. Tang, Q. Cheng, X. Wang, D. Krishnaraju, R. Panat, C. K. Chan, H. Yu, and H. Jiang, Nat. Commun. **5**, 3140 (2014).
15) Z. Y. Wei, Z. V. Guo, L. Dudte, H. Y. Liang, and L. Mahadevan, Phys. Rev. Lett. **110**, 215501 (2013).
16) C. Lv, D. Krishnaraju, G. Konjevod, H. Yu, and H. Jiang, Sci. Rep. **4**, 5979 (2014).
17) Y. Cho et al., Proc. Natl. Acad. Sci. USA **111**, 17390 (2014).
18) S. P. Lacour, J. Jones, S. Wagner, T. Li, and Z. Suo, Proc. IEEE **93**, 1459 (2005).
19) D.-H. Kim, J. Song, W. M. Choi, H.-S. Kim, R.-H. Kim, Z. Liu, Y. Y. Huang, K.-C. Hwang, Y. Zhang, and J. A. Rogers, Proc. Natl. Acad. Sci. USA **105**, 18675 (2008).
20) S. Xu et al., Nat. Commun. **4**, 1543 (2013).
21) J. Kim et al., Nat. Commun. **5**, 5747 (2014).
22) L. Xu et al., Adv. Mater. **27**, 1731 (2015).
23) C. Liu, Y. Susumago, T. Hoshi, H. Kino, T. Tanaka, and T. Fukushima, Ext. Abstr. Solid State Devices and Materials, 2022, p. 715.

24) C. Liu, T. Hoshi, H. Kino, J. Shen, A. Shinoda, Z. Du, H. Kino, T. Tanaka, and T. Fukushima, Ext. Abstr. Solid State Devices and Materials, 2023, p. 345.
25) A. Hanna et al., IEEE 68th Electronic Components and Technology Conf., 2018, p. 1505, 10.1109/ECTC.2018.00229.
26) C. Matsuda, Stretchable Film REACTIS™ Retrieved from https://xtech.nikkei.com/atcl/nxt/news/18/12504/ (2022).
27) T. Fukushima, A. Noriki, J. Bea, M. Murugesan, H. Kino, K. Kiyoyama, K.-W. Lee, T. Tanaka, and M. Koyanagi, IEEE Trans. Electron Devices **64**, 2912 (2017).
28) J.-S. Lee, Y.-J. Lee, J. Seol, Y.-C. Joo, and B.-J. Kim, Electron. Mater. Lett. **20**, 122 (2024).
29) M. Murugesan, Y. Susumago, K. Sumitani, Y. Imai, S. Kimura, and T. Fukushima, Jpn. J. Appl. Phys. **60**, SBBC02 (2021).
30) Y. Zhou, S. Sivapurapu, M. Swaminathan, and S. K. Sitaraman, IEEE Trans. Compon. Packag. Manuf. Technol. **10**, 1088 (2020).
31) T. Fukushima, A. Alam, A. Hanna, S. C. Jangam, A. A. Bajwa, and S. S. Iyer, IEEE Trans. Compon. Packag. Manuf. Technol. **8**, 1738 (2018).
32) Y. Saini, P. Singh, V. A. Arora, and K. Jain, World J. Clin. Cases **3**, 52 (2015).
33) A. Palmquist, O. M. Omar, M. Esposito, J. Lausmaa, and P. Thomsen, J. R. Soc. Interface R. Soc. **7 Suppl 5**, S515 (2010).
34) P. Chen, T. Aso, R. Sasaki, M. Ashida, Y. Tsutsumi, H. Doi, and T. Hanawa, J. Biomed. Mater. Res. A **106**, 2735 (2018).
35) Y. Wei and J. W. Hutchinson, J. Mech. Phys. Solids **45**, 1137 (1997).
36) L. C. Almeida, F. J. Echave, O. Sanz, M. A. Centeno, J. A. Odriozola, and M. Montes *Studies in Surface Science and Catalysis* ed. E. M. Gaigneaux et al., (Elsevier, Amsterdam, 2010) Vol. 175, p. 25, 10.1016/S0167-2991(10)75004-7.